American Society of Mechanical Engineers

ASME Accepted Manuscript Repository

Institutional Repository Cover Sheet

James   Zhan

First   *Last*

ASME Paper Title: Coupled Dynamics of Cable-Harnessed Structures: Experimental Validation

Authors: Karthik Yerrapragada, Armaghan Salehian

Coupled Dynamics of Cable-Harnessed Structures: Experimental Validation

Karthik Yerrapragada
PhD Candidate
Department of Mechanical and Mechatronics Engineering
University of Waterloo
Waterloo, Ontario, CANADA, N2L 3G1
email: kyerrapr@uwaterloo.ca

Armaghan Salehian, Corresponding Author
Associate Professor
Department of Mechanical and Mechatronics Engineering
University of Waterloo
Waterloo, Ontario, CANADA, N2L 3G1
email: salehian@uwaterloo.ca

Abstract

The experimental study and model validations for the coupled dynamics of a cable-harnessed beam structure is presented. The system under consideration consists of multiple pre-tensioned cables attached along the length of the host beam structure positioned at an offset distance from the beam centerline. Analytical model presented by the coupled partial differential equations (PDEs) for various coordinates of vibrations are found and the displacement frequency response functions (FRFs) obtained for both Euler-Bernoulli and Timoshenko based models are compared to those from the experiments for validation. The results are shown to be in very good agreement with the experiments.

1. Introduction

Research studies pertaining to the cable-harnessed structures and their dynamics has received lot of attention by the space industry in the past few years. For so long, the dynamic effects of the electronic and power cables on such structures were studied using ad-hoc models that involved model updating techniques to match the experimental and model results through modifications of mass, stiffness and damping properties, [1]. Applications other than space structures in which cables play an important role in the structural dynamics include power lines and marine applications, [2–4]. With the extensive use of lightweight structures in aerospace applications, obtaining a dynamic model that accurately accounts for the mass, stiffness and damping effects of these cables becomes more important,[5,6]. In this regard, Goodding et al, [5,7] have performed Finite Element Analysis (FEA) on cable-harnessed beam structures to study the bending vibrations in which they report that at lower modes, cables mass effects dominate whereas for higher modes, their damping effects become more important. Coombs et al,[8] further considers the effects of distributed mass, stiffness and damping of cables in which they are modeled as continuous beam structures using shear-beam theory analytical models. The paper reported that the shear beam

model for cables predicts better damping than the Euler-Bernoulli beam model for the bending vibrations of cable-harnessed structures. Babuska et al,[6] modeled both the host structure and the cable using Euler-Bernoulli beam theory and the model studies the bending vibrations. The paper reports that at lower modes, the cabling induces stiffening effects and at higher modes, the cable starts to resonate and also the damping effects become dominant. Ardelean et al, [9] performed FEA analysis on cable loaded plate structures and their experimental validations.

Choi et. al, [10] modeled bending vibrations of cabled structures using Timoshenko beam theory. In their theoretical model, both the host-structure and cable are modeled using beam theory and the cable is attached to the host structure using tie-down structures. The frequency response functions for the bending modes from the governing partial differential equations are obtained using the Spectral Element Method and the results are compared with the experiments. The paper concludes that the Spectral element model presented in the paper uses fewer number of discretization elements when compared to finite element modeling techniques and gives good match with the experiment. Spak et. al, [11–15] models the cables using the shear and Timoshenko beam theory and developed models to determine various effective properties of the space flight cables such as density and Young's modulus. Spak et al models both the host structures and cables using beam theory and developed mathematical models using PDEs to study the bending vibrations. They obtained the frequency response function using the Distributed Transfer Function Method (DTFM) to predict the damping induced by cabling. Spak et al, [14] also reported that when host structure is harnessed with thick space flight cables, the presence of bending-torsional modes are observed experimentally; however, their analytical model neglects the effects of coupling between various coordinates of motion such as the out of plane, in-plane bending, torsion and axial motion in the cabled structure.

With regards to the analytical modeling efforts on dynamics of cable-harnessed structures, Martin et al, [16–22] have performed extensive research in this area. They have modeled harnessing cables on host beam structures using both bar elements and string model theories to develop low order, high-fidelity distributed parameter models for bending vibrations of the cable-harnessed beam structures with periodic patterns. Their research pertains to the analytical models and experimental validations for both mass and stiffening effects of the added cables where they are wrapped around a beam structure in a periodic pattern for several geometries such as zigzag and diagonal wrapping patterns. The homogenization technique used in their work is based on the energy equivalence method similar to [23–28] to obtain PDE's for bending vibrations coordinates only. In their studies, the effects of the pre-tension of the cable and compression in the host beam structure due to pre-tension in harnessing cables are included. Other research by Martin et al, [29] considers analyzing bending vibrations of cable-harnessed beams with non-periodic wrapping patterns. All the previous research studies performed by Martin et al primarily focuses on the bending coordinates only and the coupling effects between various coordinates of vibrations are ignored in their studies.

In this regard, Yerrapragada et al [30–32], extends the work by Martin et al [16–21] to develop analytical models that include these coupling effects. Yerrapragada et al, [31] presents analytical models based on both Euler-Bernoulli and Timoshenko beam theories to study these coupling effects for a harnessed beam structure where longitudinal cables are attached along the length of a host beam structure. The energy transfer between various coordinates of vibrations are studied and the effects of various cable parameters on the system's dynamic behavior and frequencies are studied. They have shown that as the cables become dominant, these coupling behaviors are not to be neglected and must, therefore, be included in the system's dynamic modeling for better accuracy. The current paper focuses on the experimental validation of the analytical models developed in [31] for the coupled vibrations of these cable-harnessed structures. The experimentally validated coupled model is also compared to the previous modeling techniques on the decoupled vibrations by Martin et al [16–21] for accuracy. To validate each coordinate of vibration, both in-plane and out-of-plane bending tests are performed and the displacement frequency response functions for both tests are shown to identify each of these modes of vibrations. The comparisons between the coupled and previously decoupled models and the experiments clearly show the need for including these coupling effects to obtain better accuracy for the dynamic models of cable-harnessed structures.

Nomenclature

A_b	Cross sectional area of the beam
A_c	Cross sectional area of the cable
b	Width of the beam
$b_1 - b_9$	Strain energy coefficients for Euler Bernoulli-based model
$c_1 - c_{15}$	Strain energy coefficients for Timoshenko-based model
E_b	Young's Modulus of the beam
E_c	Young's modulus of the cable
G_b	Shear Modulus of the beam
h	Thickness of the beam
$k_1 - k_6$	Kinetic energy coefficients
l	Length of the beam
n	Number of cables used
r_c	Radius of the cable
T	Pre-tension of the cables
$u(x,t)$	Axial displacement
$v(x,t)$	In plane bending displacement
$w(x,t)$	Out of plane bending displacement
$w_b(t)$	Base excitation
x_a	Actuation location

x_s Sensing location

y_c y coordinate of the center of the cable ($y_c = \frac{b}{2} - \sqrt{n}.r_c$)

z_c z coordinate of the cable ($z_c = \frac{h}{2}$)

$\varphi(x,t)$ Rotation of cross-section about z axis

κ Shear Correction Factor

ρ_b Density of the beam

ρ_c Density of the cable

$\psi(x,t)$ Rotation of cross-section about y axis

$\theta(x,t)$ Torsional displacement

ω Natural Frequency

ω_f Driving frequency

2. Analytical Model

Presented in this section includes the vibrations mathematical modelling for the cable-harnessed structure shown in Figure. (1). As described before and motivated by the applications of the space structures, the beam structure considered is harnessed with a cable attached longitudinally at an offset position shown along the y-axis. As previously shown in Ref.[31], the offset position induces an asymmetry in the system that results in coupling between various coordinates of vibrations such as the out-of-plane and in-plane bending, axial and torsion. Depending on the system parameters, stronger coupling may be observed between some of the coordinates. The coupling between the coordinates results in a significant drop for the frequencies of the dominant modes of vibrations due to the stronger presence of the other modes for the coupled system as shown later in the results.

The details for the displacement field assumptions, derivations of the strain and kinetic energy expressions, the resultant governing partial differential equations, natural frequencies and mode shapes are presented in Ref.[31]. Both Euler Bernoulli and Timoshenko models are considered. For the Euler Bernoulli model, the following 4 PDEs for the coupled coordinates of vibrations for out of plane, in plane, torsional and axial modes are presented.

$$-k_1 \ddot{u} + b_1 u'' + b_6 v''' + b_7 w'''_{rel} = 0 \tag{1a}$$

$$-k_2 \ddot{v} - b_2 v'''' - b_6 u''' - b_5 w''''_{rel} + b_9 \theta'' = 0 \tag{1b}$$

$$-k_3 \ddot{w}_{rel} - b_3 w''''_{rel} - b_7 u''' - b_5 v'''' + b_8 \theta'' = k_3 \ddot{w}_b \tag{1c}$$

$$-k_4 \ddot{\theta} + b_4 \theta'' + b_9 v'' + b_8 w''_{rel} = 0 \tag{1d}$$

The boundary conditions associated with the fixed and free ends are shown in the Appendix Equations. (A.1) and (A.2) respectively.

where $u(x,t), v(x,t), w_{rel}(x,t), \theta(x,t)$ are the motions in the axial, in-plane bending, out-of-plane bending and torsion respectively. Also, $w_b(t)$ is the base excitation provided to the cantilevered structure in the out of plane bending direction. Therefore, w_{rel} is the relative out of plane bending motion of any point on the structure with respect to the base. Superscript $(\;)'$ denotes partial derivative with respect to spatial coordinate and superscript $(\dot{\;})$ denotes partial derivative with respect to time. The coefficients for the Euler-Bernoulli model partial differential equations (Equations 1 (a) – 1(d)) are shown in the Appendix (Equation. (A.3)).

Similarly, the governing partial differential equations of motion along with the boundary conditions for the Timoshenko model can be found as, [31].

$$-k_1\ddot{u} + c_1 u'' + c_8\varphi'' + c_9\psi'' = 0 \tag{2a}$$

$$-k_2\ddot{v} + c_2 v'' + c_{12}\theta'' + c_{11}\varphi' = 0 \tag{2b}$$

$$-k_3\ddot{w}_{rel} + c_3 w''_{rel} + c_{13}\theta'' + c_{15}\psi' = k_3\ddot{w}_b \tag{2c}$$

$$-k_4\ddot{\theta} + c_4\theta'' + c_{12}v'' + c_{13}w''_{rel} = 0 \tag{2d}$$

$$-k_5\ddot{\varphi} + c_5\varphi'' - c_7\varphi + c_8 u'' - c_{11}v' + c_{10}\psi'' = 0 \tag{2e}$$

$$-k_6\ddot{\psi} + c_6\psi'' - c_{14}\psi + c_9 u'' - c_{15}w'_{rel} + c_{10}\varphi'' = 0 \tag{2f}$$

The boundary conditions for the fixed and free ends for these are also listed in the Appendix. Equations. (A.4) and (A.5) respectively.

where $u(x,t), v(x,t), w_{rel}(x,t), \theta(x,t), \psi(x,t), \varphi(x,t)$, are the motions in the axial, in-plane bending, out-of-plane bending, torsion, rotations of the cross-section about y and z axes respectively. The coefficients in Equation (2) are listed in the Appendix (Equation. (A.6)).

Next, the solutions to the PDEs above are found to obtain the natural frequencies and mode shapes and ultimately the frequency response functions, in particular the one for the out-of-plane bending, for experimental validations is shown in Equation (3)

$$W(\omega_f) = \left| \frac{1}{\omega_f^2} + \sum_{i=1}^{\infty} \frac{k_3.W_{i,rel}(x = x_s).\int_{x=0}^{l} W_{i,rel}(x)\,dx}{\omega_i^2 - \omega_f^2} \right| \tag{3}$$

Here, x_s is the sensing location, ω_f is the excitation frequency and ω_i is the natural frequency associated with the ith mode. Also, $W_{i,rel}(x = x_s)$ is the relative mass normalized mode shape value of the ith mode at the sensing location for the out-of-plane bending.

3. Experimental Setup and Results

 Figure. (2) shows the experimental setup for the cable harnessed system under the base excitations. The system consists of 10 pre-tensioned cables attached to the host structure as shown. The host structure is a beam made of Aluminum 6061 alloy and the cable is an 80-pound strength Power Pro Super 8 Slick fishing line. The material and geometrical properties are presented in Table. (1). A 2075E The Modal Shop electrodynamic shaker and a 2050E09 The Modal Shop power amplifier are used to provide the excitations. To control the acceleration profile for the shaker base excitations, a PicoCoulomB (PCB) accelerometer 352A24 and Siemens LMS 05 Mobile (SCM) Supervisory Control And Data Acquisition System (SCADAS) data acquisition unit are used. This data acquisition system is also used to obtain the frequency response functions. A Polytec OFV-5000 laser vibrometer controller and Polytec OFV-505 sensor head are used for vibration measurements.

 The structure is mounted on the shaker as shown in Figure. (2) and is subjected to the sine sweep base excitations in the out-of-plane bending direction (z-axis) from 15 to 500 Hz using the Siemens LMS Sine Control Module. The frequency response functions are measured in the out-of-plane bending direction as well. In order to make sure that the added tape to attach the cables to the beam has not resulted in any noticeable dynamic effects, the experimental frequency response functions for the host beam structure without any cables both before and after adding the tape are measured and shown in Figure. (3). The FRFs comparison for the two systems clearly indicates that the added tape has no noticeable effect on the host beam structure's dynamics. It is, therefore, expected that the tape used for attaching the cables will have no measurable dynamic impact on the cable-harnessed system either.

 Further as a sanity check, the experimental frequency response function for the host beam structure with the added tape is compared to the analytical results for the host beam structure with no tape or cable. The good match between the two shown in Figure. (4) further proves that the added tape has no noticeable effect on the dynamics of the host beam structure and, therefore, it can be ignored in the rest of the analysis for the cable harnessed beam structure as well.

 Next step involves obtaining the experimental frequency response functions for the cable-harnessed beam structure with pre-tensioned cables. Modular weights are used to apply the cable pre-tension while the unit is being assembled. The cables are attached at an offset distance along the y-axis as shown in Figure. (2). The cables are twisted together and closer view of the cable bundle is presented in Figure. (2c). The total pre-tension applied is 17.22 N for the 10 cables attached. The base excitations for the cable harnessed beam to obtain the FRFs are performed at two different sensing locations, 95 mm and 248 mm. Shown in Figure. (5) is the cross-sectional area of the n cables bundled together; here $n=10$. The total cross-sectional area of the n cables can be found using Equation. (4). This area is equivalent to that of a circle with $\sqrt{n}.r_c$ radius as shown

in Figure. (5). Using this diagram, it can be easily understood how y_c and z_c coordinates of the point of attachment of the cable to the beam are found. This is the point P where the strain value for the cables is evaluated. It is assumed that the cables remain attached to the top surface of the beam at all times and, therefore, will have the same strain values as the beam top fiber. It is also assumed that the entire bundle of cables experiences the same strain values. This assumption includes further corrections to Martin et al. [18] where the strain was previously evaluated at the center of the cable using the beam strain distribution function.

$$A = n.\pi r_c{}^2 = \pi(\sqrt{n}.r_c)^2 \tag{4}$$

The frequency response functions obtained from the experiments are compared to the theoretical results for each of the Euler Bernoulli and Timoshenko coupled models presented in this paper as well as the previously decoupled Euler Bernoulli model, [18]. The comparison of the theory and experimental results for the two sensing locations are presented in Figures. (6) and (7). As clearly demonstrated in these figures, significant improvement is observed for the present coupled model in comparison to the previous decoupled model particularly for the higher modes. Also, in the frequency range shown, apart from the three significant peaks corresponding to the out-of-plane bending dominant modes, there exists a small peak at around 147.1 Hz. This peak corresponds to the in-plane bending, whose presence is well-predicted by the coupled modeling approach while the decoupled system is only capable of predicting the out-of-plane bending modes.

To better observe the details of the FRFs comparisons, the zoom-in plots around each mode are shown in Figures. (8) and (9) for both sensing locations. The reason for overestimating the natural frequencies by the previous decoupled model, [18], is due to ignoring the compliance in the other coordinates of vibrations as also discussed in [31]. Since in the decoupled model only the out-of-plane bending coordinate is considered, this implies that the structure is assumed to be rigid in all the other directions of motion preventing it from vibrating in those directions. This overestimation of the overall stiffness of the structure results in the frequencies to be overestimated as well. Therefore, introducing the other coordinates of vibrations in the model is a more realistic assumption that results in a more accurate representation of the system's overall stiffness and natural frequencies compared to their experimental values. Additionally, the coupled model accounts for the energy transfer between various coordinates of vibrations that ultimately results in lowering of the out-of-plane bending frequency estimations compared to the decoupled system, [31]. Also shown in the experimental FRFs for the out-of-plane measurement is a small peak at 147.1 Hz. This mode pertains to the in-plane bending coordinate which is difficult to observe in the out-of-plane direction of measurement. To further investigate this mode, the in-plane bending impact hammer tests are also performed for the two sets of actuation and sensing locations shown in Figure. (10) and the FRFs are presented in Figures. (11a) and (11b). Subscripts *'a1, a2'* and *'s1, s2'* denote the actuation and sensing locations in Figure. (10) respectively. An impact hammer

model number PicoCoulomB (PCB) 086C01 with a metal tip is used for this test. Both the impact excitation and sensing are done in the in-plane direction shown in Figure (10). A total number of 5 averages are taken for each of the impact tests for which the coherence plots are also presented in Figure. (12) for each of the impact test. The very dominant peak shown at about 147 Hz frequency for both these FRF plots further indicate that this mode corresponds to an in-plane bending mode. Also, shown in these plots (Figure. (11)) are the small peaks at about 22 Hz and 133 Hz, both corresponding to the out-of-plane bending modes that are not as obvious due to being in the other direction. Both experimental and their corresponding theoretical frequency values for all the modes are tabulated and shown in Table. (2) for comparison. Also, the sharp peak at around 178 Hz in the FRFs from the model corresponds to the coupled model estimation for the in-plane bending frequency. To further prove this, the theoretical mode shapes are also plotted at this frequency and shown in Figure. (13). From the mass normalized amplitude values for each of these coordinates' mode shapes at this frequency, it can be observed that this mode is clearly an in-plane dominant mode. The mode shape also indicates the first in-plane bending mode. The error values shown in Table. (2) further indicate the improvement made for using the coupled model when compared to the previous decoupled model. Also, the Euler-Bernoulli and Timoshenko results line up perfectly showing that for the system parameters considered in this case study. However, for thicker beam specimen the Timoshenko model assumptions should be used for better accuracy.

4. Conclusions

In this paper, experimental validations for the coupled model to present the vibrations response of a cable-harnessed beam structure are performed. The system consisted of a bundle of pre-tensioned cables attached along the length of the host structure at an offset position. Base excitations are provided to the structure in the out-of-plane bending direction to obtain the FRFs. The frequency response functions for both the coupled and decoupled analytical models are then compared to the experimental values. The results for the coupled model are shown to be in very good agreement with the experimental results clearly indicating the need for including the coupling effects between various coordinates of vibrations in the model.

Acknowledgements

References

[1]   Robertson, L., Lane, S., Ingram, B., Hansen, E., Babuska, V., Goodding, J., Mimovich, M., Mehle, G., Coombs, D., and Ardelean, E., 2007, "Cable Effects on the Dynamics of Large Precision Structures," *48th AIAA/ASME/ASCE/AHS/ASC Structures, Structural Dynamics, and Materials Conference*, p. 2389.

[2]   McClure, G., and Lapointe, M., 2003, "Modeling the Structural Dynamic Response of Overhead Transmission Lines," Computers & Structures, **81**(8–11), pp. 825–834.

[3]   Witz, J. A., and Tan, Z., 1992, "On the Axial-Torsional Structural Behaviour of Flexible Pipes, Umbilicals and Marine Cables," Marine Structures, **5**(2–3), pp. 205–227.

[4]   Huang, S., 1999, "Stability Analysis of the Heave Motion of Marine Cable-Body Systems," Ocean Engineering, **26**(6), pp. 531–546.

[5]   Goodding, J., Babuska, V., Griffith, D. T., Ingram, B., and Robertson, L., 2007, "Studies of Free-Free Beam Structural Dynamics Perturbations Due to Mounted Cable Harnesses," *48th AIAA/ASME/ASCE/AHS/ASC Structures, Structural Dynamics, and Materials Conference*, p. 2390.

[6]   Babuska, V., Coombs, D. M., Goodding, J. C., Ardelean, E. V, Robertson, L. M., and Lane, S. A., 2010, "Modeling and Experimental Validation of Space Structures with Wiring Harnesses," Journal of Spacecraft and Rockets, **47**(6), pp. 1038–1052.

[7]   Goodding, J. C., Ardelean, E. V, Babuska, V., Robertson, L. M., and Lane, S. A., 2011, "Experimental Techniques and Structural Parameter Estimation Studies of Spacecraft Cables," Journal of Spacecraft and Rockets, **48**(6), pp. 942–957.

[8]   Coombs, D. M., Goodding, J. C., Babuška, V., Ardelean, E. V, Robertson, L. M., and Lane, S. A., 2011, "Dynamic Modeling and Experimental Validation of a Cable-Loaded Panel," Journal of Spacecraft and Rockets, **48**(6), pp. 958–974.

[9]   Ardelean, E., Goodding, J., Coombs, D., Griffee, J., Babuška, V., Robertson, L., and Lane, S., 2010, "Cable Effects Study: Tangents, Rat Holes, Dead Ends, and Valuable Results," *51st AIAA/ASME/ASCE/AHS/ASC Structures, Structural Dynamics, and Materials Conference 18th AIAA/ASME/AHS Adaptive Structures Conference 12th*, p. 2806.

[10]   Choi, J., and Inman, D. J., 2014, "Spectrally Formulated Modeling of a Cable-Harnessed Structure," Journal of sound and vibration, **333**(14), pp. 3286–3304.

[11]   Spak, K., Agnes, G., and Inman, D., 2014, "Parameters for Modeling Stranded Cables as Structural Beams," Experimental Mechanics, **54**(9), pp. 1613–1626.

[12]   Spak, K., Agnes, G., and Inman, D., 2014, "Cable Parameters for Homogenous Cable-Beam Models for Space Structures," *Dynamics of Civil Structures, Volume 4*, Springer, pp. 7–18.

[13]   Spak, K. S., Agnes, G. S., and Inman, D. J., 2014, "Bakeout Effects on Dynamic Response of Spaceflight Cables," Journal of Spacecraft and Rockets, **51**(5), pp. 1721–1734.

[14]   Spak, K. S., 2014, "Modeling Cable Harness Effects on Spacecraft Structures.", PhD thesis, Virginia Tech.

[15]   Spak, K. S., Agnes, G. S., and Inman, D., 2013, "Towards Modeling of Cable-Harnessed Structures: Cable Damping Experiments," *54th AIAA/ASME/ASCE/AHS/ASC Structures, Structural Dynamics, and Materials Conference*, p. 1889.

[16]   Martin, B., and Salehian, A., 2014, "Vibration Modelling of String-Harnessed Beam Structures Using Homogenization Techniques," *ASME 2014 International Mechanical*

Engineering Congress and Exposition, American Society of Mechanical Engineers, p. V04BT04A074-V04BT04A074.

[17] Martin, B., and Salehian, A., 2013, "Vibration Analysis of String-Harnessed Beam Structures: A Homogenization Approach," *54th AIAA/ASME/ASCE/AHS/ASC Structures, Structural Dynamics, and Materials Conference*, p. 1892.

[18] Martin, B., and Salehian, A., 2016, "Mass and Stiffness Effects of Harnessing Cables on Structural Dynamics: Continuum Modeling," AIAA Journal, pp. 2881–2904.

[19] Martin, B., and Salehian, A., 2016, "Homogenization Modeling of Periodically Wrapped String-Harnessed Beam Structures: Experimental Validation," AIAA Journal, pp. 3965–3980.

[20] Martin, B., and Salehian, A., 2013, "Dynamic Modelling of Cable-Harnessed Beam Structures with Periodic Wrapping Patterns: A Homogenization Approach," International Journal of Modelling and Simulation, **33**(4), pp. 185–202.

[21] Martin, B., and Salehian, A., 2013, "Cable-Harnessed Space Structures: A Beam-Cable Approach," *24th International Association of Science and Technology for Development International Conference on Modelling and Simulation*, ACTA Press Calgary, AB, Canada, pp. 280–284.

[22] Martin, B., and Salehian, A., 2017, "String-Harnessed Beam Structures: An Inverse Problem Approach for Model Approximation." *International Conference on Inverse Problems in Engineering,* Waterloo, ON, Canada.

[23] Salehian, A., Seigler, T. M., and Inman, D. J., 2007, "Dynamic Effects of a Radar Panel Mounted on a Truss Satellite," AIAA journal, **45**(7), pp. 1642–1654.

[24] Salehian, A., Cliff, E. M., and Inman, D. J., 2006, "Continuum Modeling of an Innovative Space-Based Radar Antenna Truss," Journal of Aerospace Engineering, **19**(4), pp. 227–240.

[25] Salehian, A., and Inman, D. J., 2008, "Dynamic Analysis of a Lattice Structure by Homogenization: Experimental Validation," Journal of Sound and Vibration, **316**(1–5), pp. 180–197.

[26] Salehian, A., Inman, D. J., and Cliff, E. M., 2006, "Natural Frequency Validation of a Homogenized Model of a Truss," *Proceedings of the XXIV-International Modal Analysis Conference*.

[27] Salehian, A., and Inman, D. J., 2010, "Micropolar Continuous Modeling and Frequency Response Validation of a Lattice Structure," Journal of Vibration and Acoustics, **132**(1), p. 11010.

[28] Salehian, A., and Chen, Y., 2012, "On Strain-Rate Dependence of Kinetic Energy in Homogenization Approach: Theory and Experiment," AIAA journal, **50**(10), pp. 2029–2033.

[29] Martin, B., and Salehian, A., 2018, "Continuum Modeling of Nonperiodic String-Harnessed Structures: Perturbation Theory and Experiments," AIAA Journal, pp. 1–16.

[30] Yerrapragada, K., and Salehian, A., 2018, "Coupled Axial, In Plane and Out of Plane Bending Vibrations of Cable Harnessed Space Structures," *International Conference on Applied Mathematics, Modeling and Computational Science*, Springer, Waterloo, ON, Canada, pp. 249–257.

[31] Yerrapragada, K., and Salehian, A., 2019, "Analytical Study of Coupling Effects for Vibrations of Cable-Harnessed Beam Structures," Journal of Vibration and Acoustics. **141**(3)**,** p. 031001.

[32] Yerrapragada, K., and Salehian, A., 2018, "Coupled Bending, Torsion and Axial Vibrations of a Cable-Harnessed Beam With Periodic Wrapping Pattern," *IDETC Conference*, ASME, Quebec city, Quebec, Canada, pp. 1–8.

List of Figures

Figure. 1 Schematic of the cable-harnessed beam and the coordinate axes.

Figure. 2 Base excitation experimental setup for the cantilevered cable harnessed beam, (a) beam structure, accelerometer and shaker, (b) laser vibrometer controller, sensor head, power amplifier, and LMS data acquisition system, (c) closer view of the cable bundle.

Figure. 3 Experimental displacement frequency response functions from shaker tests for host beam structure + tape and no cables and host beam structure without tape at $x_s=95\ mm$ sensing location.

Figure. 4 Comparison between the displacement frequency response function from shaker test of host beam structure + tape and host beam structure without tape analytical model at $x_s=95\ mm$ sensing location.

Figure. 5 Schematic of beam width view and cable offset position.
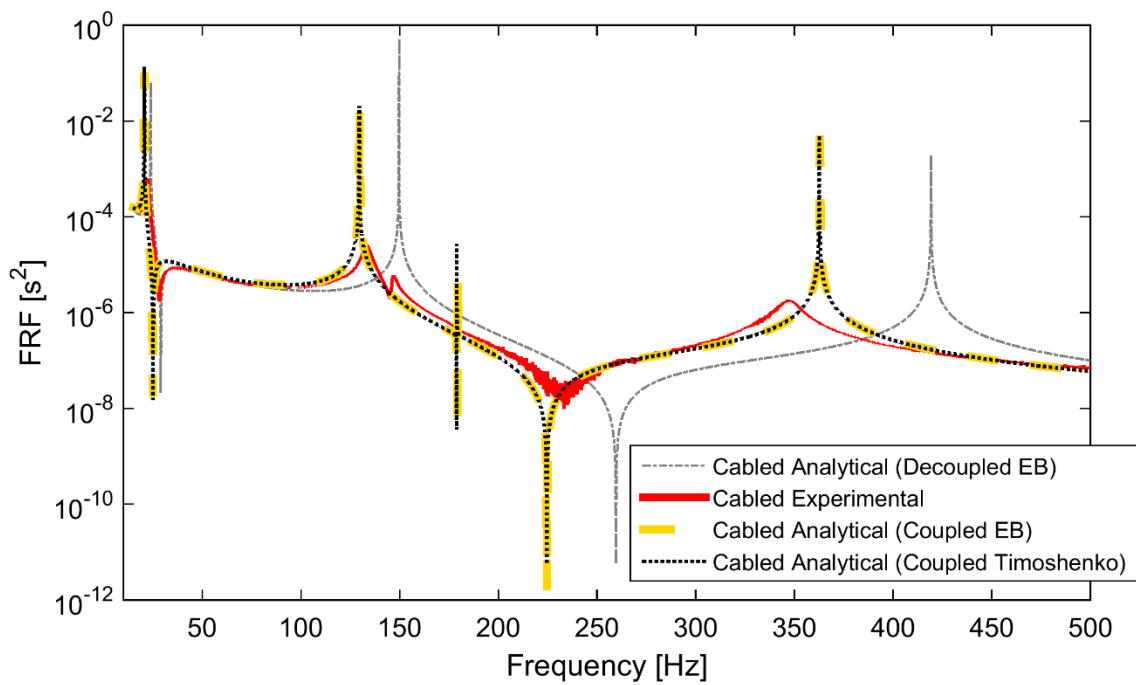
Figure. 6 Comparison of the cable harnessed displacement frequency response functions from shaker experiment, decoupled and coupled analytical models for $x_s=95\ mm$.
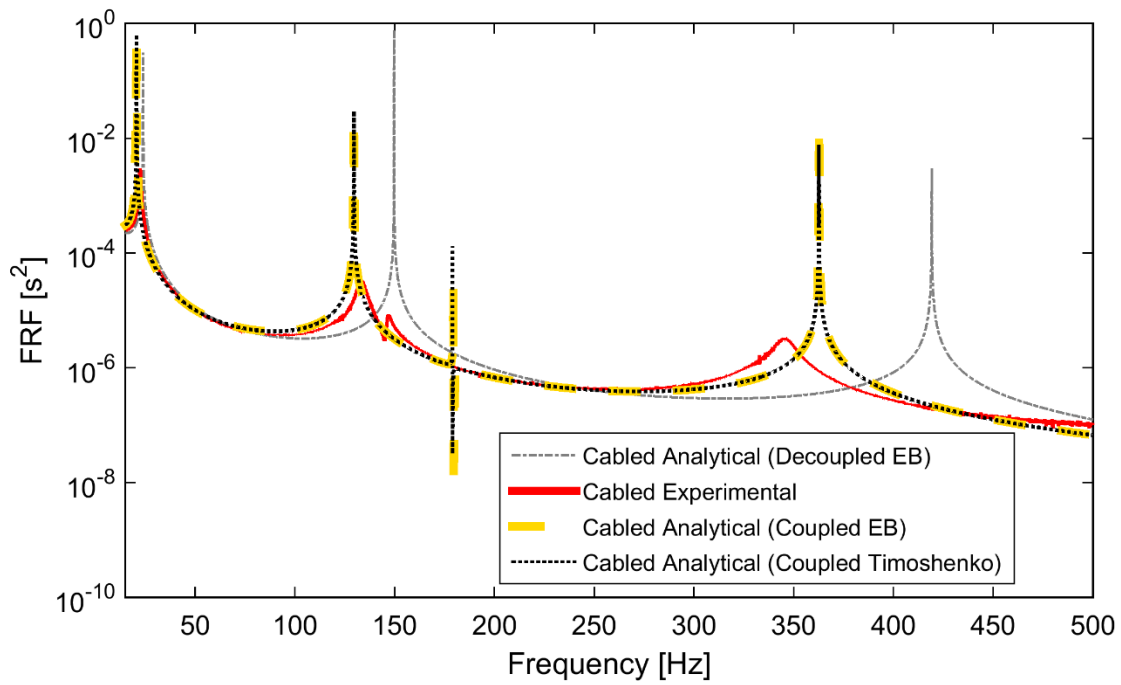
Figure. 7 Comparison of the cable harnessed displacement frequency response functions from shaker experiment, decoupled and coupled analytical models for $x_s=248\ mm$.

Figure. 8 Zoom in plots for displacement frequency response functions for shaker experiment, coupled and decoupled models of $x_s=95\ mm$ for a) Mode 1 b) Modes 2 and 3 and c) Mode 4.

Figure. 9 Zoom in plots for displacement frequency response functions for shaker experiment, coupled and decoupled models of $x_s=248\ mm$ for a) Mode 1 b) Modes 2 and 3 and c) Mode 4.

Figure. 10 Sensing and actuation locations for the two in-plane impact hammer tests.

Figure. 11 Displacement frequency response functions for in-plane impact tests. a) impact test for $(x_{a1},\ x_{s1}) = (55,\ 95)\ mm$, b) impact test for $(x_{a2},\ x_{s2}) = (31,\ 248)\ mm$.

Figure. 12 Coherence plots for the in-plane impact hammer tests. $(x_{a1},\ x_{s1}) = (55,\ 95)\ mm$, (b) $(x_{a2},\ x_{s2}) = (31,\ 248)\ mm$.

Figure. 13 First in-plane bending dominant mode shape from the coupled analytical model. U, V, W, θ denote the axial, in-plane bending, out-of-plane bending and torsional mode shapes at the first in-plane dominant mode respectively.
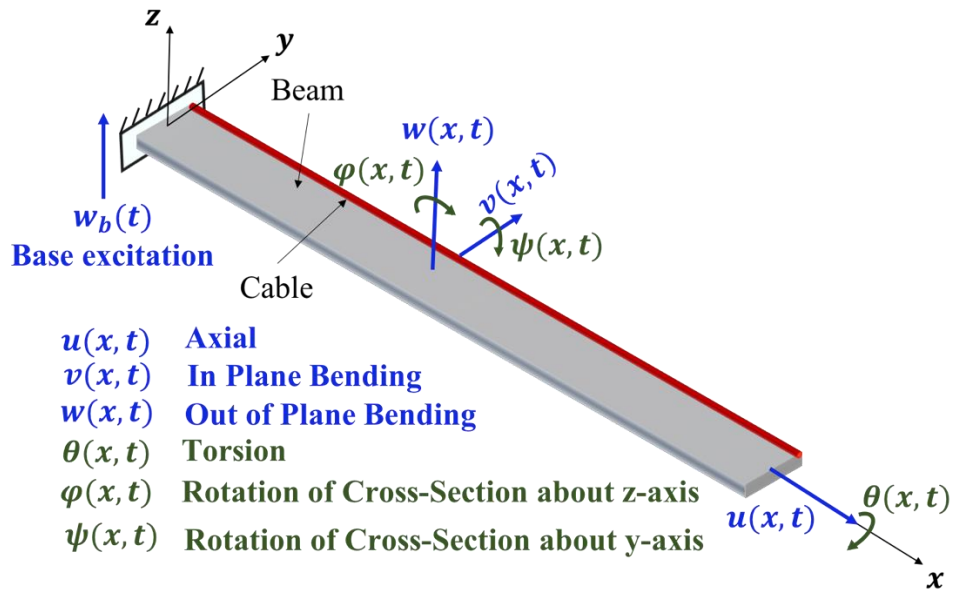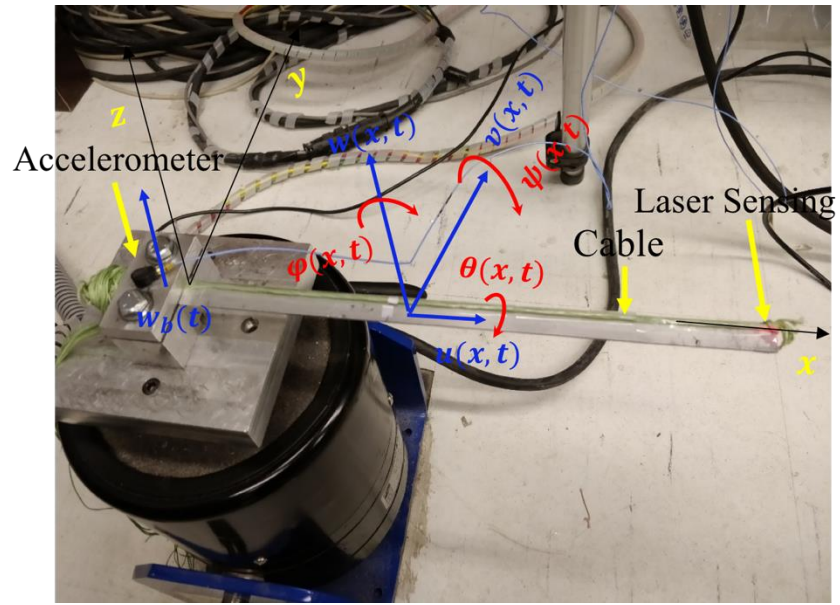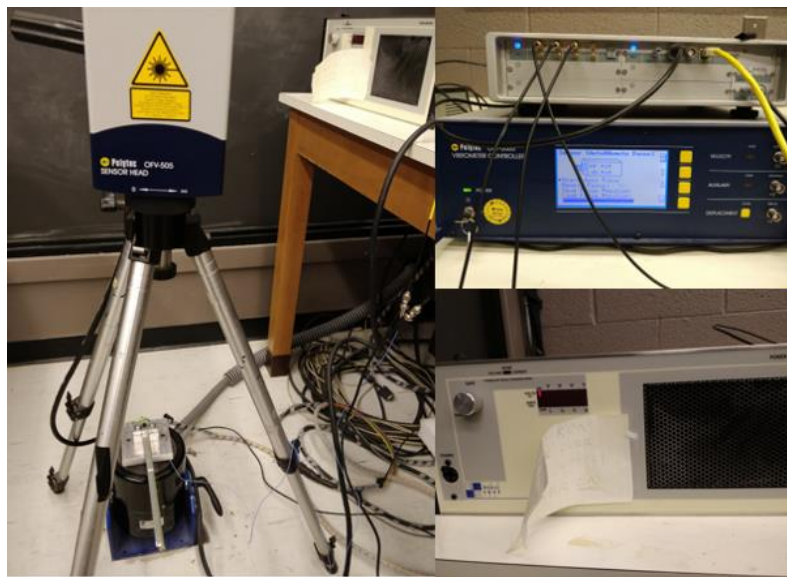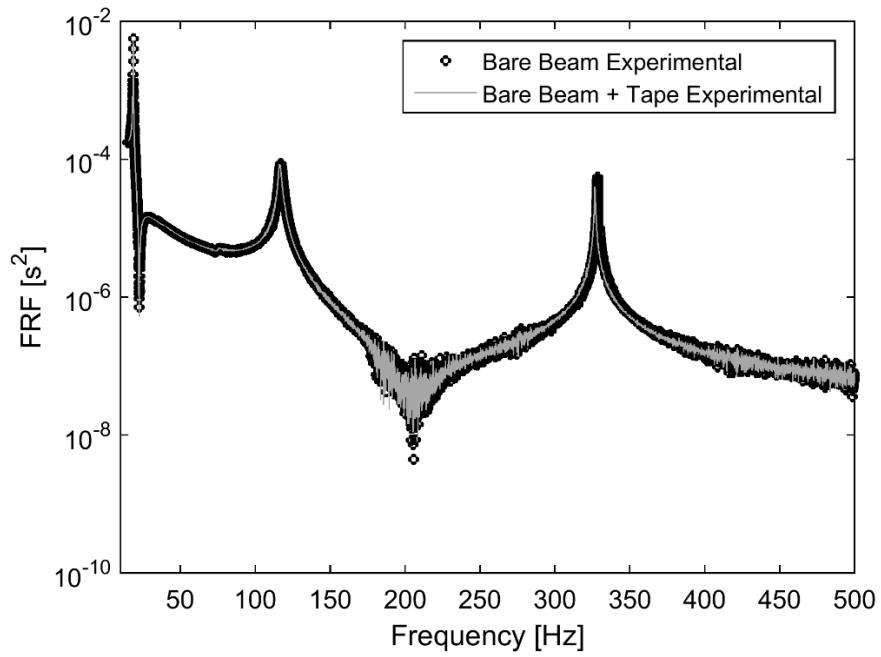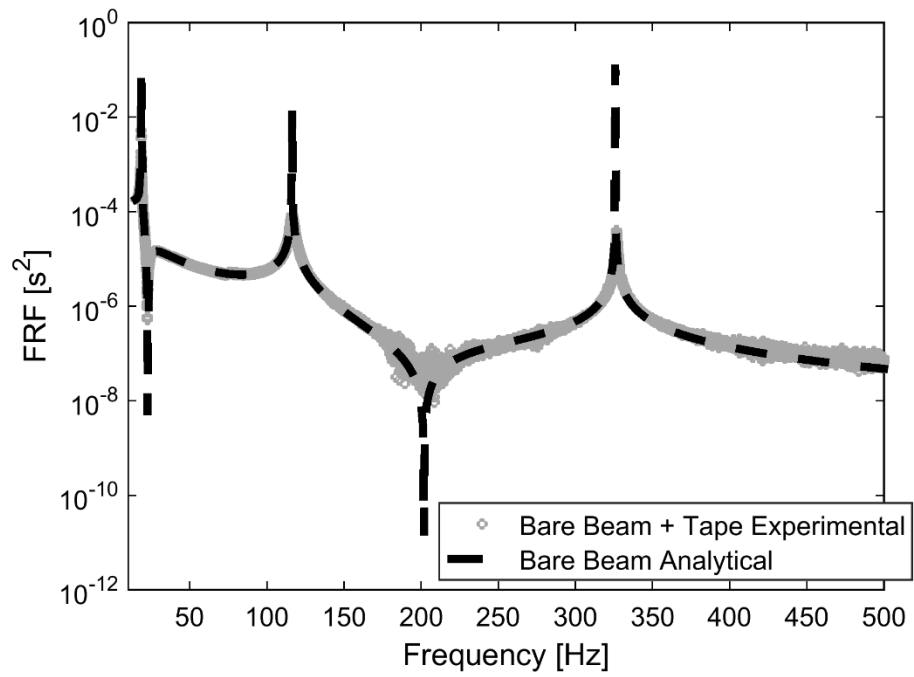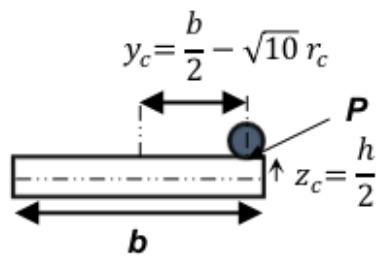
Figure. 1 Schematic of the cable-harnessed beam and the coordinate axes.

(a)

(b)

(c)

Figure. 2 Base excitation experimental setup for the cantilevered cable harnessed beam, (a) beam structure, accelerometer and shaker, (b) laser vibrometer controller, sensor head, power amplifier, and LMS data acquisition system, (c) closer view of the cable bundle.

Figure. 3 Experimental displacement frequency response functions from shaker tests for host beam structure + tape and no cables and host beam structure without tape at x_s=95 mm sensing location.

Figure. 4 Comparison between the displacement frequency response function from shaker test of host beam structure + tape and host beam structure without tape analytical model at $x_s=95\ mm$ sensing location.

$$y_c = \frac{b}{2} - \sqrt{10}\, r_c$$

$$z_c = \frac{h}{2}$$

Figure. 5 Schematic of beam width view and cable offset position.

Figure. 6 Comparison of the cable harnessed displacement frequency response functions from shaker experiment, decoupled and coupled analytical models for x_s=95 mm.

Figure. 7 Comparison of the cable harnessed displacement frequency response functions from shaker experiment, decoupled and coupled analytical models for x_s=248 mm.
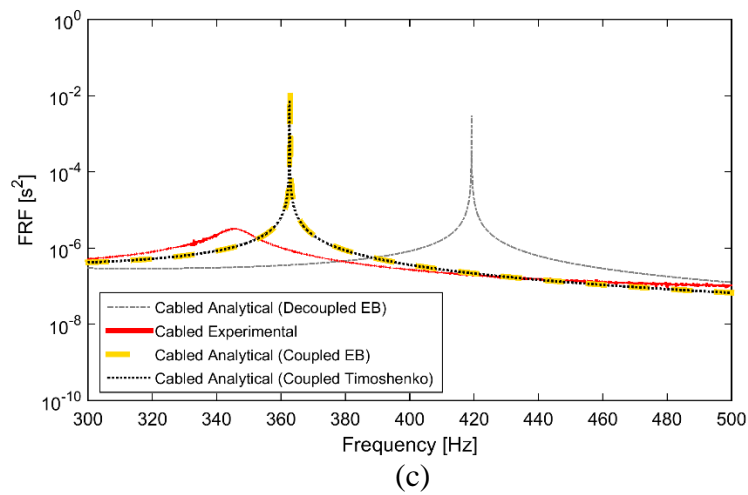
Figure. 8 Zoom in plots for displacement frequency response functions for shaker experiment, coupled and decoupled models of $x_s=95\ mm$ for a) Mode 1 b) Modes 2 and 3 and c) Mode 4.
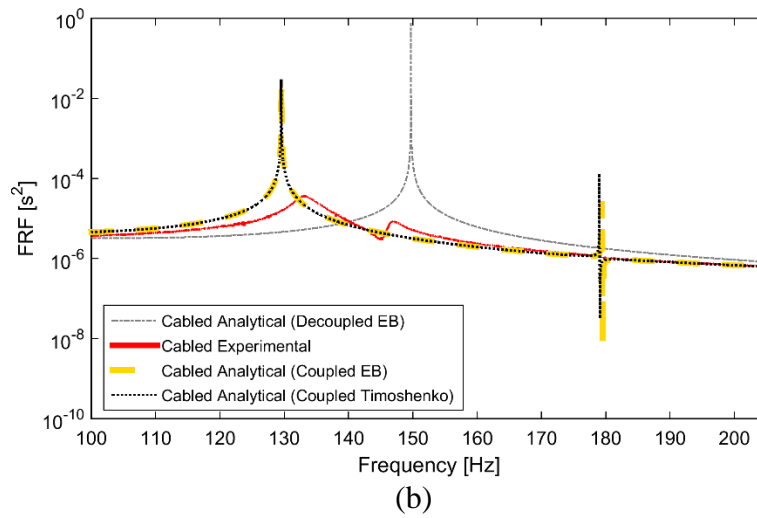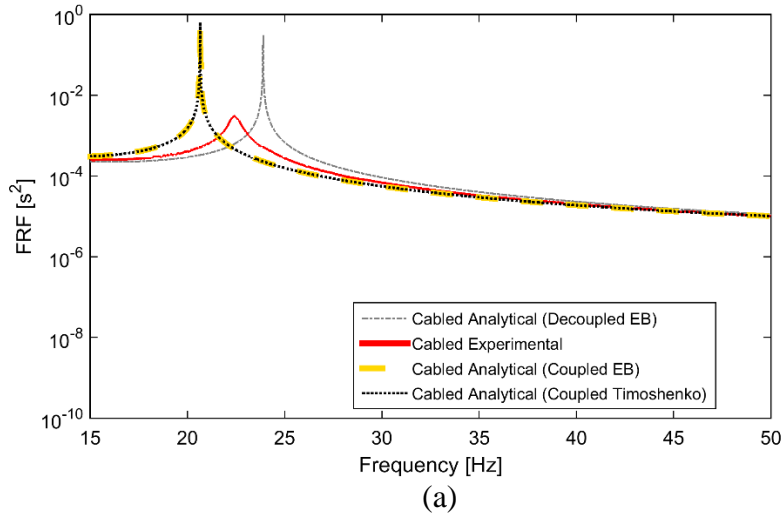
(a)

(b)

(c)

Figure. 9 Zoom in plots for displacement frequency response functions for shaker experiment, coupled and decoupled models of $x_s=248\ mm$ for a) Mode 1 b) Modes 2 and 3 and c) Mode 4.
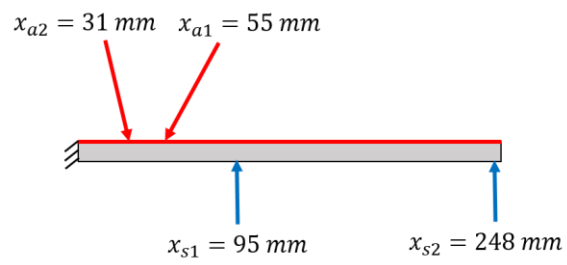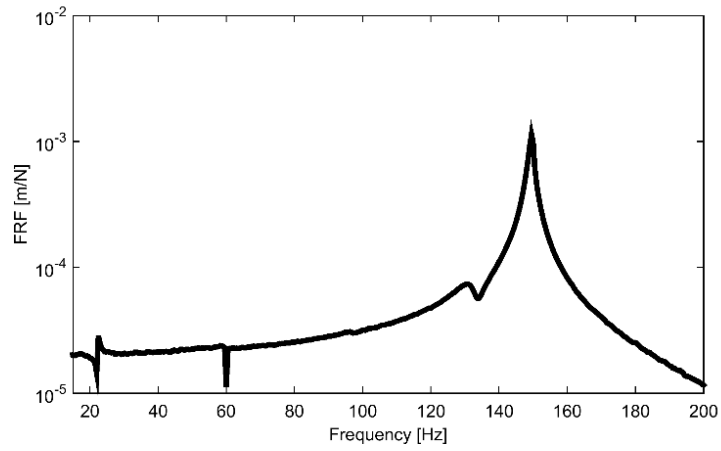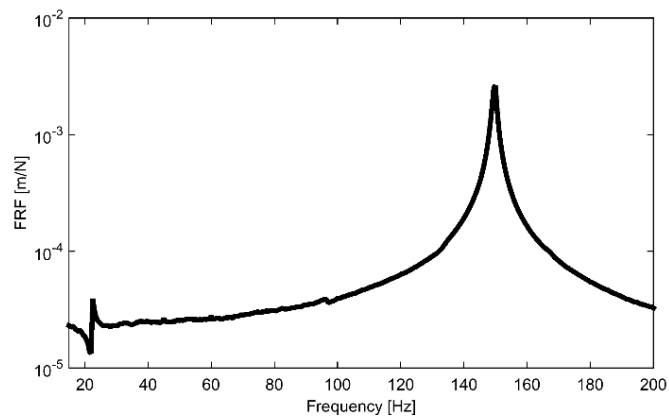
Figure. 10 Sensing and actuation locations for the two in-plane impact hammer tests.

Figure. 11 Displacement frequency response functions for in-plane impact tests. a) impact test for $(x_{a1}, x_{s1}) = (55, 95)$ *mm*, b) impact test for $(x_{a2}, x_{s2}) = (31, 248)$ *mm*.
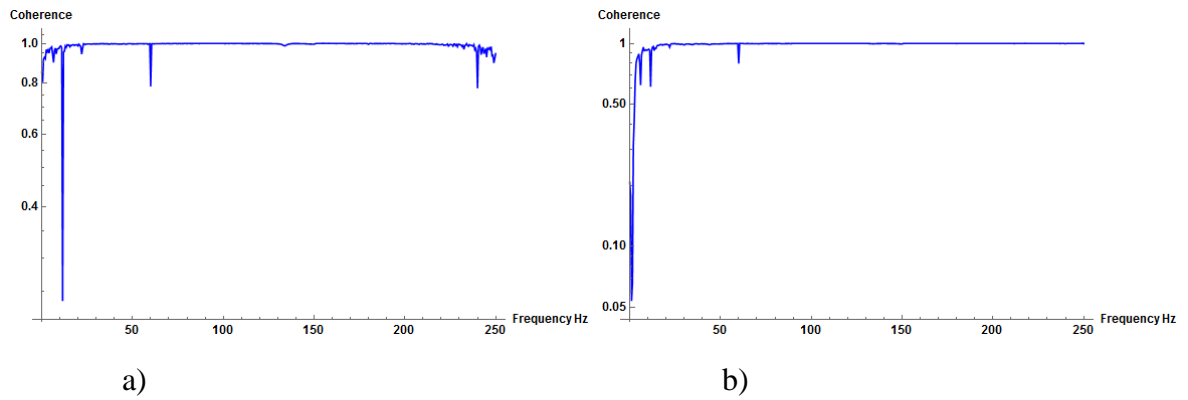
Figure. 12 Coherence plots for the in-plane impact hammer tests. $(x_{a1}, x_{s1}) = (55, 95)$ *mm,* (b) $(x_{a2}, x_{s2}) = (31, 248)$ *mm.*
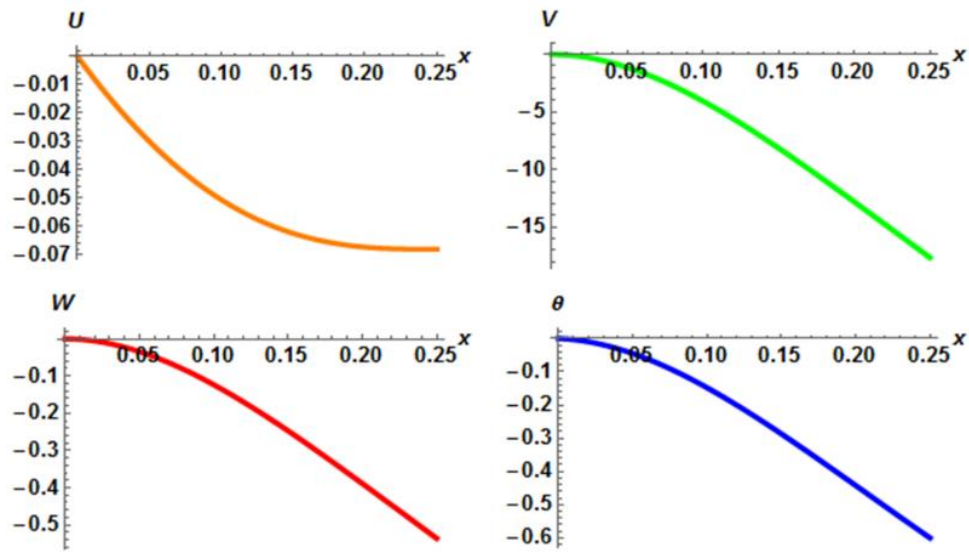
Figure. 13 First in-plane bending dominant mode shape from the coupled analytical model. U, V, W, θ denote the axial, in-plane bending, out-of-plane bending and torsional mode shapes at the first in-plane dominant mode respectively.

List of Tables

Table. 1 Material and geometrical properties of the cable harnessed beam structure.

System parameters	Value
Beam length	0.25 m
Beam width	0.01243 m
Beam thickness	0.00144 m
Beam density	2,768 Kg/m^3
Beam modulus of elasticity	68.9 GPa
Beam Shear modulus	25.7 GPa
Pre-tension of the cables	17.22 N
Cable radius (per cable)	0.00021 m
Cable density	1,400 Kg/m^3
Cable modulus of elasticity	128.04 GPa
Number of Cables	10

Table. 2 Natural frequencies for analytical and experimental models for cabled harnessed beam.

Mode	Decoupled Euler-Ber. [Hz]	Coupled Euler-Ber. [Hz]	Coupled Timoshenko [Hz]	Experiment [Hz]	Error % Decoupled	Error % Coupled Euler-Ber.	Error % Coupled Timoshenko
1	23.88	20.65	20.65	22.35 (OP)	6.84 %	-7.60 %	-7.60 %
2	149.70	129.56	129.53	133.2 (OP)	12.38 %	-2.73 %	-2.75 %
3	-	179.42	178.99	147.1 (IP)	-	21.97 %	21.67 %
4	419.23	362.85	362.65	345.6 (OP)	21.30 %	4.99 %	4.93 %

*OP and IP refer to the out-of-plane and in-plane bending modes respectively.

Appendix

Shown below are the equations used for the boundary conditions and the coefficients in the PDE's of the given systems.

Fixed end

$$u = v = w_{rel} = \theta = v' = w_{rel}' = 0|_{x=0} \tag{A.1}$$

Free end.

$$b_1 u' + b_6 v'' + b_7 w''_{rel} = 0|_{x=l}$$

$$b_2 v'' + b_5 w''_{rel} + b_6 u' = 0|_{x=l}$$

$$b_2 v''' + b_5 w'''_{rel} + b_6 u'' - b_9 \theta' = 0|_{x=l} \tag{A.2}$$

$$b_3 w''_{rel} + b_5 v'' + b_7 u' = 0|_{x=l}$$

$$b_3 w'''_{rel} + b_5 v''' + b_7 u'' - b_8 \theta' = 0|_{x=l}$$

$$b_4 \theta' + b_8 w'_{rel} + b_9 v' = 0|_{x=l}$$

Equations. (A.1) and (A.2) are the boundary conditions for the fixed and free ends for the PDEs corresponding to the Euler-Bernoulli cable-harnessed model (Equation. (1)).

$$b_1 = E_b A_b + E_c A_c \qquad\qquad b_8 = T y_c$$

$$b_2 = E_b I_{zz} + E_c A_c y_c{}^2 + T y_c{}^2 - \frac{T I_{zz}}{A_b}$$

$$b_9 = -T z_c$$

$$b_3 = E_b I_{yy} + E_c A_c z_c{}^2 + T z_c{}^2 - \frac{T I_{yy}}{A_b} \qquad k_1 = \rho_b A_b + \rho_c A_c$$

$$b_4 = G_b J + T(y_c{}^2 + z_c{}^2) - \frac{T J}{A_b} \qquad k_2 = \rho_b A_b + \rho_c A_c \tag{A.3}$$

$$b_5 = E_c A_c y_c z_c + T y_c z_c \qquad\qquad k_3 = \rho_b A_b + \rho_c A_c$$

$$b_6 = (E_c A_c + T)(-y_c) \qquad\qquad k_4 = \rho_b I_{xx} + \rho_c A_c (y_c{}^2 + z_c{}^2)$$

$$b_7 = (E_c A_c + T)(-z_c)$$

Equation. (A.3) represents the coefficients of PDEs Equation. (1) for Euler-Bernoulli model. where, I_{yy} and I_{zz} are the area moments of inertia of the beam about the y and z axes respectively. J is the torsion constant of the beam. polar inertia $I_{xx} = I_{yy} + I_{zz}$. Other notations are defined in the nomenclature table.

Fixed end

$$u = v = w_{rel} = \theta = \varphi = \psi = 0|_{x=0} \tag{A.4}$$

Free end

$$c_1 u' + c_8 \varphi' + c_9 \psi' = 0|_{x=l}$$

$$c_2 v' + c_{11}\varphi + c_{12}\theta' = 0|_{x=l}$$

$$c_3 w'_{rel} + c_4 \theta' + c_{15}\psi = 0|_{x=l}$$

$$c_4 \theta' + c_{12} v' + c_{13} w'_{rel} = 0|_{x=l} \tag{A.5}$$

$$c_5 \varphi' + c_8 u' + c_{10}\psi' = 0|_{x=l}$$

$$c_6 \psi' + c_9 u' + c_{10}\varphi' = 0|_{x=l}$$

Equations. (A.4) and (A.5) are the boundary conditions for the fixed and free ends for the PDEs corresponding to the Timoshenko cable-harnessed model (Equation. (2)).

$$c_1 = E_b A_b + E_c A_c \qquad\qquad c_{12} = -z_c T$$

$$c_2 = \kappa A_b G_b \qquad\qquad c_{13} = y_c T$$

$$c_3 = \kappa A_b G_b \qquad\qquad c_{14} = \kappa A_b G_b$$

$$c_4 = G_b J + T(y_c{}^2 + z_c{}^2) - \frac{TJ}{A_b} \qquad\qquad c_{15} = \kappa A_b G_b$$

$$\qquad\qquad\qquad\qquad\qquad\qquad\qquad\qquad\qquad\qquad\qquad \tag{A.6}$$

$$c_5 = E_c A_c y_c{}^2 + T y_c{}^2 + E_b I_{zz} - \frac{TI_{zz}}{A_b} \qquad k_1 = \rho_b A_b + \rho_c A_c$$

$$c_6 = E_c A_c z_c{}^2 + T z_c{}^2 + E_b I_{yy} - \frac{TI_{yy}}{A_b} \qquad k_2 = \rho_b A_b + \rho_c A_c$$

$$c_7 = \kappa A_b G_b \qquad\qquad k_3 = \rho_b A_b + \rho_c A_c$$

$$c_8 = -E_c A_c y_c - T y_c \qquad\qquad k_4 = \rho_b I_{xx} + \rho_c A_c (y_c{}^2 + z_c{}^2)$$

$$c_9 = E_c A_c z_c + T z_c \qquad\qquad k_5 = \rho_b I_{zz} + \rho_c A_c (y_c{}^2)$$

$$c_{10} = (E_c A_c + T)(-y_c z_c) \qquad\qquad k_6 = \rho_b I_{yy} + \rho_c A_c (z_c{}^2)$$

$$c_{11} = -\kappa A_b G_b$$

Equation. (A.6) represents the coefficients of partial differential equations Equation. (2) for the Timoshenko model. Notations are defined in the nomenclature table and also for the discussion related to Equation. (A.3).